Research Square

Preprints are preliminary reports that have not undergone peer review.
They should not be considered conclusive, used to inform clinical practice,
or referenced by the media as validated information.

Precipitant-Dosage Regulation of Spinel-Type (FeCoMnCuZn) 3 O 4 High-Entropy Oxide for High-Performance Asymmetric Supercapacitors

Zijing Tian
Dalian Jiaotong University
Fanen Zeng
Dalian Jiaotong University
Yuhan Liang
Dalian Jiaotong University
Zilong Zhou
Dalian Jiaotong University
Bing Xu
xb@djtu.edu.cn

Dalian Jiaotong University

Research Article

Keywords: Supercapacitors, High-entropy oxides, Spinel structure, Coprecipitation, Sodium carbonate

Posted Date: August 6th, 2026

DOI: https://doi.org/10.21203/rs.3.rs-10544266/v1

License: This work is licensed under a Creative Commons Attribution 4.0 International License.
Read Full License

Additional Declarations: No competing interests reported.

Precipitant-Dosage Regulation of Spinel-Type $(FeCoMnCuZn)_3O_4$ High-Entropy Oxide for High-Performance Asymmetric Supercapacitors

Zijing Tian[a], Fanen Zeng[b], Yuhan Liang[a], Zilong Zhou[a], Bing Xu[*b]

a School of Transportation Engineering, Dalian Jiaotong University, Dalian, 116028, China

b School of Materials Science and Engineering, Dalian Jiaotong University, Dalian, 116028, China

Abstract

High-entropy oxides (HEOs) have emerged as promising electrode materials for supercapacitors owing to their compositional tunability, robust crystal structures, multicomponent synergistic effects, and excellent structural stability. In this work, spinel-type $(FeCoMnCuZn)_3O_4$ HEO was synthesized via a facile coprecipitation strategy followed by air calcination. The effects of precipitant type and Na_2CO_3 dosage on the phase structure, particle morphology, elemental distribution, surface valence states, and electrochemical performance were systematically investigated. The sample prepared with 10 mmol Na_2CO_3 exhibited a single-phase spinel structure, relatively high crystallinity, uniform nanoparticle morphology, and homogeneous multimetal elemental distribution. XPS analysis confirmed the coexistence of multivalent Fe, Co, Mn, and Cu species, together with oxygen-vacancy-related defects, which are beneficial for charge transfer and reversible Faradaic reactions. Benefiting from the optimized microstructure and compositional synergy, the 10 mmol electrode delivered a specific capacitance of 416.4 F g^{-1} at 1 A g^{-1} and retained 207.4 F g^{-1} at 20 A g^{-1}. Furthermore, an asymmetric supercapacitor assembled using $(FeCoMnCuZn)_3O_4$ as the positive electrode and activated carbon as the negative electrode operated stably within a 1.4 V voltage window, achieving an energy density of 46.94 Wh kg^{-1} at

750 W kg^{-1} and maintaining 12.06 Wh kg^{-1} at 15000 W kg^{-1}. After 5000 cycles at 5 A g^{-1}, a capacitance retention of 87.23% was retained. This work demonstrates that precipitant-dosage regulation is an effective strategy for optimizing the microstructure and electrochemical performance of high-entropy spinel oxides.

Keywords: Supercapacitors; High-entropy oxides; Spinel structure; Coprecipitation; Sodium carbonate

Introduction

The rapid development of renewable-energy systems, portable electronic devices, and electric vehicles has created an increasing demand for electrochemical energy-storage devices with high power density, rapid charge/discharge capability, long cycle life, and reliable safety [1][2]. Supercapacitors have attracted extensive attention because they bridge the performance gap between conventional dielectric capacitors and rechargeable batteries. According to their charge-storage mechanisms, supercapacitors are generally classified as electric double-layer capacitors, pseudocapacitors, and hybrid/asymmetric supercapacitors [3]. Among these systems, pseudocapacitive and hybrid devices are particularly attractive because reversible Faradaic reactions can provide higher capacitance and energy density than pure double-layer charge storage. However, the relatively low energy density and insufficient cycling durability of many electrode materials still hinder practical application. Therefore, the design of advanced electrode materials with abundant redox-active sites, rapid ion/electron transport pathways, and stable crystalline structures remains essential for high-performance supercapacitors [4][5].

Transition-metal oxides, sulfides, nitrides, phosphides, and carbon-based composites have been widely explored as supercapacitor electrode materials because of their tunable compositions

and diverse charge-storage behaviors [6]. In particular, transition-metal oxides can store charge through reversible surface or near-surface redox reactions. Nevertheless, conventional single-metal and binary oxides often suffer from poor intrinsic conductivity, limited active sites, insufficient phase stability, and structural degradation during repeated charge/discharge processes [5]. High-entropy materials provide a promising strategy for overcoming these limitations by incorporating multiple principal elements into a single-phase solid-solution structure. Their high configurational entropy, lattice distortion, sluggish diffusion effect, and cocktail effect can endow electrode materials with enhanced structural stability, tunable electronic structures, and multiple redox centers [7][8].

Among various high-entropy materials, spinel-type high-entropy oxides are particularly suitable for supercapacitor applications because their AB_2O_4 frameworks can accommodate multiple transition-metal cations at both tetrahedral and octahedral sites. The coexistence of multivalent metal species, such as Fe^{2+}/Fe^{3+}, Co^{2+}/Co^{3+}, Mn^{3+}/Mn^{4+}, Cu^{2+}/Cu^{+}, and Zn^{2+}, can facilitate reversible Faradaic reactions in alkaline electrolytes. Meanwhile, oxygen vacancies generated by charge compensation may serve as additional electroactive sites and accelerate charge transfer. However, the electrochemical performance of high-entropy spinel oxides is strongly dependent on the synthesis strategy, precursor homogeneity, particle size, crystallinity, pore structure, and surface chemical state [9]. Therefore, sol-gel [17,18,19,20], coprecipitation [11,12,13], hydrothermal [14,15,16], solid-state, combustion, spray-pyrolysis, template-assisted, and chemical-vapor-deposition methods have been developed to regulate the microstructure and electrochemical kinetics of HEOs [21,22,23].

Several representative HEO systems have recently been reported for supercapacitor

applications. Talluri et al. synthesized spinel-type $(CoCrFeMnNi)_3O_4$ nanoparticles by a reverse-coprecipitation method and demonstrated their potential as pristine spinel HEO electrodes; the electrode delivered 239 F g^{-1} at 0.5 A g^{-1} and retained 76% of its initial capacitance after 1000 cycles [24]. Zhang et al. prepared HEO electrodes by a dealloying method, achieving a specific capacitance of 639 F g^{-1} at 1 A g^{-1} with 80.77% capacitance retention [25]. Yin et al.[26] introduced polyethylene glycol as a pore-forming agent to construct porous $(FeCoCrMnNi)_3O_4$ high-entropy ceramic powders with a specific surface area of 92.76 m^2 g^{-1}; the optimized electrode delivered 204 F g^{-1} at 0.5 A g^{-1}, and the assembled asymmetric device achieved 53 Wh kg^{-1} at 400.8 W kg^{-1} .

In addition to spinel oxides, other high-entropy structures and morphology-control strategies have been investigated. Wang et al. developed a MOF-gel method to synthesize porous $La(Mn_{0.2}Fe_{0.2}Co_{0.2}Ni_{0.2}Cu_{0.2})O_3$ high-entropy perovskite nanoparticles with abundant mesopores; the optimized electrode exhibited 609.3 F g^{-1} at 1 A g^{-1}, and the assembled solid-state HEO//AC device delivered 31.2 Wh kg^{-1} with 84.2% capacitance retention after 10000 cycles [27]. Arun and Jacob investigated spinel-type $(MnFeCoNiZn)_3O_4$ nanoparticles for supercapacitor applications, confirming the feasibility of Zn-containing HEO electrodes [28]. Despite these advances, several issues remain unresolved. First, many high-performance HEOs are based on Cr^- and/or Ni-containing systems, whereas Fe-Co-Mn-Cu-Zn spinel compositions remain insufficiently investigated. Second, although template-assisted, MOF-derived, and surfactant-assisted strategies can effectively tailor pore structures, they usually require additional organic templates, multistep processing, or relatively complex synthesis conditions [27,33]. Third, although the importance of precipitant selection has been recognized [29,30], the influence of carbonate dosage on precursor

precipitation, crystallinity, particle growth, elemental homogeneity, and electrochemical behavior has not been fully clarified. Either excessive or insufficient CO_3^{2-} concentration may alter the coprecipitation rates of different metal ions, thereby affecting precursor uniformity, final oxide crystallinity, and ion-accessible active sites. Therefore, optimization of the carbonate precipitation process provides a simple and effective approach for tuning high-entropy spinel oxide electrodes.

In this work, spinel-type $(FeCoMnCuZn)_3O_4$ HEO was synthesized by a coprecipitation method, and the effects of precipitant type and dosage on the structural characteristics and electrochemical performance of the as-prepared HEOs were systematically investigated. An asymmetric supercapacitor assembled with the optimized HEO as the positive electrode and commercial activated carbon (AC) as the negative electrode exhibited favorable capacitance, energy-density, and power-density performance.**2. Experimental Section**

2.1 Materials

Ferric sulfate hydrate ($Fe_2(SO_4)_3 \cdot 7H_2O$), cobalt sulfate heptahydrate ($CoSO_4 \cdot 7H_2O$), manganese sulfate monohydrate ($MnSO_4 \cdot H_2O$), copper sulfate pentahydrate ($CuSO_4 \cdot 5H_2O$), zinc sulfate heptahydrate ($ZnSO_4 \cdot 7H_2O$), sodium carbonate (Na_2CO_3), sodium hydroxide (NaOH), and sodium bicarbonate ($NaHCO_3$) were used as received without further purification. The exact hydrate state and purity of each metal salt should be verified and reported according to the supplier information.

2.2 Synthesis of $(FeCoMnCuZn)_3O_4$

Equimolar amounts of Fe, Co, Mn, Cu, and Zn salts (1 mmol for each metal ion) were dissolved in deionized water under magnetic stirring to form a homogeneous mixed-metal solution. For precipitant screening, Na_2CO_3, $NaHCO_3$, or NaOH was slowly added to the solution at a

precipitant/total-metal-cation molar ratio of 2:1 to initiate coprecipitation. For $Na2CO_3$-dosage optimization, the Na_2CO_3/total-metal-cation molar ratios were adjusted to 1.8:1, 2.0:1, and 2.2:1, corresponding to Na_2CO_3 additions of 9, 10, and 11 mmol, respectively. After standing for 12 h, the precipitates were collected by centrifugation, washed repeatedly to remove soluble impurities, and dried to obtain precursor powders. The obtained precursors were calcined in air at 900 °C for 2 h in a muffle furnace and then naturally cooled to room temperature. The final products were ground into fine powders for subsequent structural and electrochemical characterization.

2.3 Characterization

The crystal structures of the samples were analyzed by X-ray diffraction (XRD) using a PANalytical Empyrean diffractometer with Cu Kα radiation (λ = 1.54056 Å) operated at 45 kV and 40 mA. Diffraction patterns were recorded over a 2θ range of 10-80° at a scanning rate of 5° min^{-1}. The particle morphology, size distribution, agglomeration state, and microstructure were observed using a Zeiss SUPRA 55 field-emission scanning electron microscope (SEM). Transmission electron microscopy (TEM), high-resolution TEM (HRTEM), selected-area electron diffraction (SAED), and energy-dispersive X-ray spectroscopy (EDS) mapping were performed using a JEOL JEM-2100F field-emission transmission electron microscope. X-ray photoelectron spectroscopy (XPS) was conducted on an ESCALAB 250Xi spectrometer to determine the surface elemental composition and chemical valence states.

2.4 Electrochemical measurements

Nickel foam substrates were sequentially ultrasonicated in hydrochloric acid, absolute ethanol, and deionized water for 10 min each to remove surface contaminants. After drying, the initial mass was recorded as m_1. The HEO powder, BP2000 carbon black, and

polytetrafluoroethylene (PTFE) emulsion were mixed at a mass ratio of 8:1:1 and ground into a homogeneous slurry. The slurry was coated onto nickel foam and dried at 60 °C for 12 h. The mass of the dried electrode was recorded as m_2, and the effective active-material loading was calculated as $M = (m_2 - m_1) \times 0.8$. The active-material loading was approximately 2 mg cm^{-2}. The coated nickel foam was pressed with a nickel tab at 10 MPa before electrochemical testing.

Electrochemical measurements were carried out using a three-electrode configuration with the as-prepared electrode as the working electrode, a Hg/HgO electrode as the reference electrode, and a platinum mesh as the counter electrode. An asymmetric supercapacitor (ASC) was assembled using the HEO electrode as the positive electrode, activated carbon as the negative electrode, 2 M KOH as the electrolyte, and a cellulose membrane as the separator. Cyclic voltammetry (CV), galvanostatic charge-discharge (GCD), and electrochemical impedance spectroscopy (EIS) were used to evaluate the electrochemical performance.In the three-electrode and two-electrode systems, the calculation formulas for specific capacitance C (F g^{-1}) are respectively [30]

$$C=\frac{I\Delta t}{m\Delta V} \tag{1}$$

$$C_s=\frac{2I\Delta t}{m\Delta V} \tag{2}$$

In the formula, m is the mass of the active material (g), I is the discharge current (A), Δt is the discharge time (s), and ΔV is the voltage range (V).

The energy density (E) and power density (P) are calculated according to Equation [31].

$$E=\frac{C\times\Delta v}{2\times3.6} \tag{3}$$

$$p=\frac{3600\times E}{\Delta t} \tag{4}$$

In the equation, E, P, C, ΔV, and Δt represent the energy density (Wh kg^{-1}), power density (W

kg^{-1}), specific capacitance (F g^{-1}), voltage window (V), and discharge time (s) of the ASC, respectively.

To investigate the diffusion of ions and electrons during the charge-discharge process, the relationship between the peak current (i) of the anode and cathode and the scan rate (v) can be derived using the following formula [32]:

$$i=av^b \tag{5}$$

$$\log i = \log a + b \log v \tag{6}$$

Among them, i is the current density (A g^{-1}), v is the scan rate (mV s^{-1}), and a and b are adjustable parameters. The value of b can be calculated from the slope of the linear plot. The contributions of the capacitive effect and the diffusion-controlled process to the scan rate can be calculated according to the following formula [33]:

$$i=k_1 v+k_2 \log v^{\frac{1}{2}} \tag{7}$$

where k_1 represents the capacitive effect, and k_2 represents the diffusion effect.

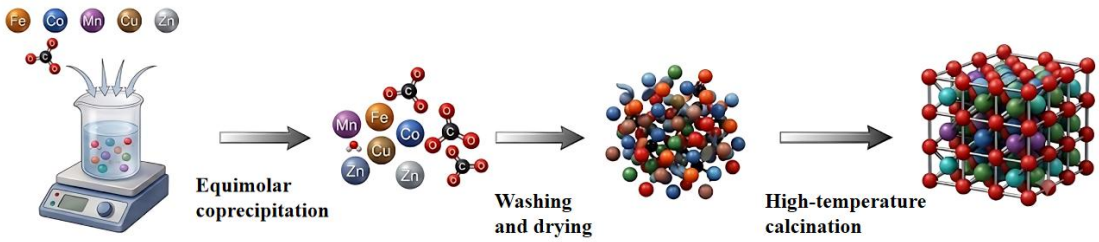


Figure 1. Schematic diagram of the synthesis strategy for porous HEOs.

3. Results and Discussion

XRD analysis shows that the $(FeCoMnCuZn)_3O_4$ HEOs prepared with different precipitants exhibit a single-phase spinel structure consistent with the PDF#34-1400 standard card, without detectable impurity phases. Diffraction peaks located at 2θ values of 18.3°, 30.1°, 35.4°, 37.1°, 43.1°, 53.4°, 57.0°, and 62.6° are indexed to the (111), (220), (311), (222), (400), (422), (511), and

(440) planes of the spinel structure, respectively. As shown in Fig. 2(a), the sample prepared using Na_2CO_3 exhibits stronger and sharper diffraction peaks than those prepared with $NaHCO_3$ and NaOH, indicating improved crystallinity. When the Na_2CO_3 dosage is varied, the 10 mmol sample shows the strongest diffraction intensity and the narrowest full width at half maximum for the main (311) peak, suggesting the highest crystallinity. In contrast, the 9 mmol sample shows weaker and broader peaks, probably because insufficient precipitant leads to incomplete metal-ion precipitation and poorer precursor homogeneity. Increasing the Na_2CO_3 dosage to 11 mmol does not further improve crystallinity, which may be attributed to excessively rapid precipitation at high CO_3^{2-} concentration, leading to less uniform multication dispersion in the precursor.

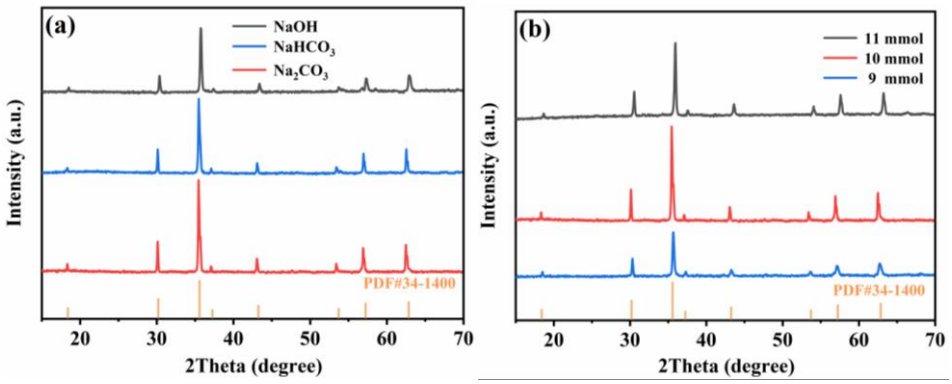


Figure 2. (a) XRD patterns of $(FeCoMnCuZn)_3O_4$ prepared with different precipitants. (b) XRD patterns of samples with different Na_2CO_3 addition amounts.

SEM images of the samples prepared with different Na_2CO_3 dosages are shown in Fig. 3. At 9 mmol, irregular particles with a broad size distribution and pronounced agglomeration are observed. When the Na_2CO_3 dosage is increased to 10 mmol, finer nanoparticles with a more uniform size distribution and reduced agglomeration are obtained, and the particles are packed in a relatively loose manner. Further increasing the Na_2CO_3 dosage to 11 mmol results in significant particle growth and the formation of regular polyhedral block-like particles with clear crystal

facets and relatively smooth surfaces. Although this morphology suggests improved crystal growth, the larger particle size and denser packing are unfavorable for electrolyte-ion diffusion and active-site accessibility.

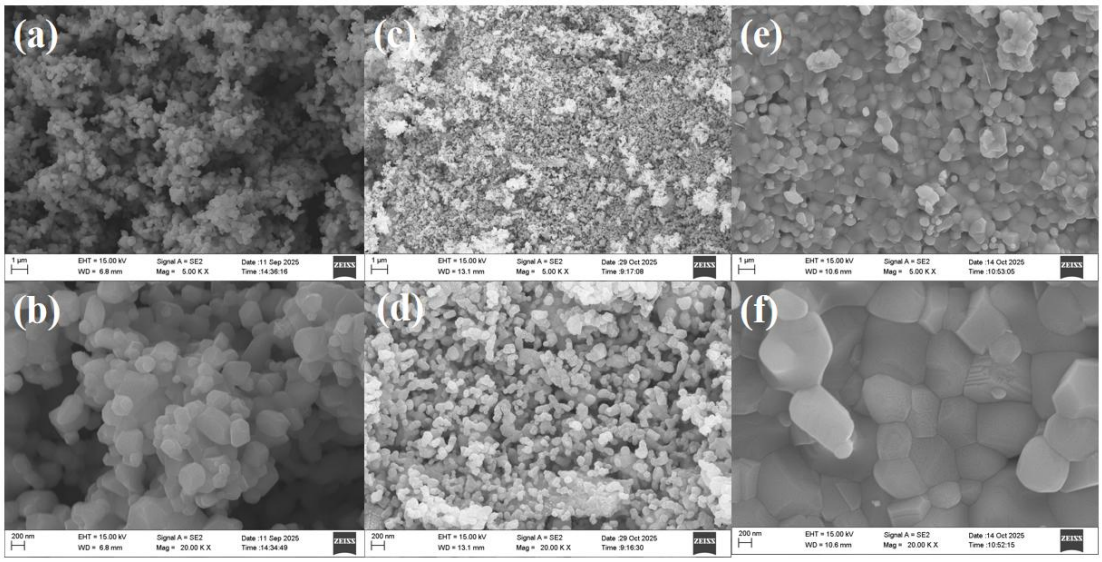


Figure 3. SEM images of samples prepared with different Na_2CO_3 dosages: (a, b) 9 mmol, (c, d) 10 mmol, and (e, f) 11 mmol.

TEM analysis of the 10 mmol sample further confirms its nanoparticulate morphology. As shown in Fig. 4(a), the sample consists mainly of irregular nanoparticles with partial aggregation, consistent with the SEM observations. Clear lattice fringes are observed in the HRTEM image (Fig. 4(b)), indicating good crystallinity. The measured interplanar spacing of approximately 0.296 nm corresponds to the characteristic (220) plane of the spinel structure. The SAED pattern (Fig. 4(c)) displays sharp concentric diffraction rings that can be assigned to the (111), (220), and (311) planes, demonstrating the polycrystalline nature of the product. EDS elemental mapping (Figs. 4(d-j)) reveals that Fe, Co, Mn, Cu, Zn, and O are homogeneously distributed throughout the selected region, indicating that no obvious elemental segregation occurred during synthesis.

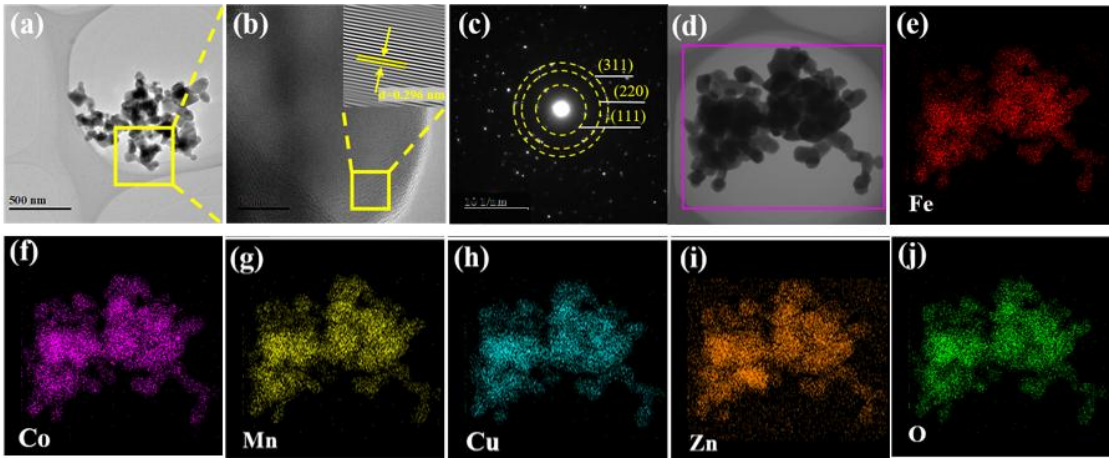


Figure 4. Characterization of the 10 mmol sample: (a) low-magnification TEM image, (b) HRTEM image, (c) SAED pattern, and (d-j) EDS elemental maps of Fe, Co, Mn, Cu, Zn, and O.

The surface chemical states of the optimized 10 mmol sample were investigated by high-resolution XPS. As shown in Fig. 5(a), the Fe 2p spectrum contains characteristic components associated with Fe^{2+} and Fe^{3+}, together with satellite peaks, confirming the coexistence of mixed Fe valence states. In the Co 2p spectrum (Fig. 5(b)), the Co $2p_{3/2}$ region can be deconvoluted into Co^{3+} and Co^{2+} components, accompanied by corresponding Co $2p_{1/2}$ peaks and satellite features. These results indicate that Co exists in mixed Co^{2+}/Co^{3+} states. The Mn 2p spectrum (Fig. 5(c)) reveals the coexistence of Mn^{3+} and Mn^{4+} species, suggesting that reversible Mn redox transitions may contribute to charge storage. In the Cu 2p spectrum (Fig. 5(d)), the main Cu $2p_{3/2}$ and Cu $2p_{1/2}$ peaks, along with pronounced shake-up satellite peaks, indicate that Cu is mainly present as Cu^{2+}. The Zn 2p spectrum (Fig. 5(e)) shows two characteristic peaks corresponding to Zn $2p_{3/2}$ and Zn $2p_{1/2}$, indicating the presence of Zn^{2+}. Although Zn^{2+} contributes little direct pseudocapacitance, it can help stabilize the spinel framework and modulate the local electronic environment. The O 1s spectrum (Fig. 5(f)) is fitted into lattice oxygen (O_L), oxygen-vacancy/defect oxygen (O_V), and surface-adsorbed oxygen/hydroxyl species (O_C). The oxygen-vacancy-related component suggests the presence of oxygen defects, which may facilitate

charge transfer and cooperate with multivalent metal species to enhance reversible Faradaic reactions.

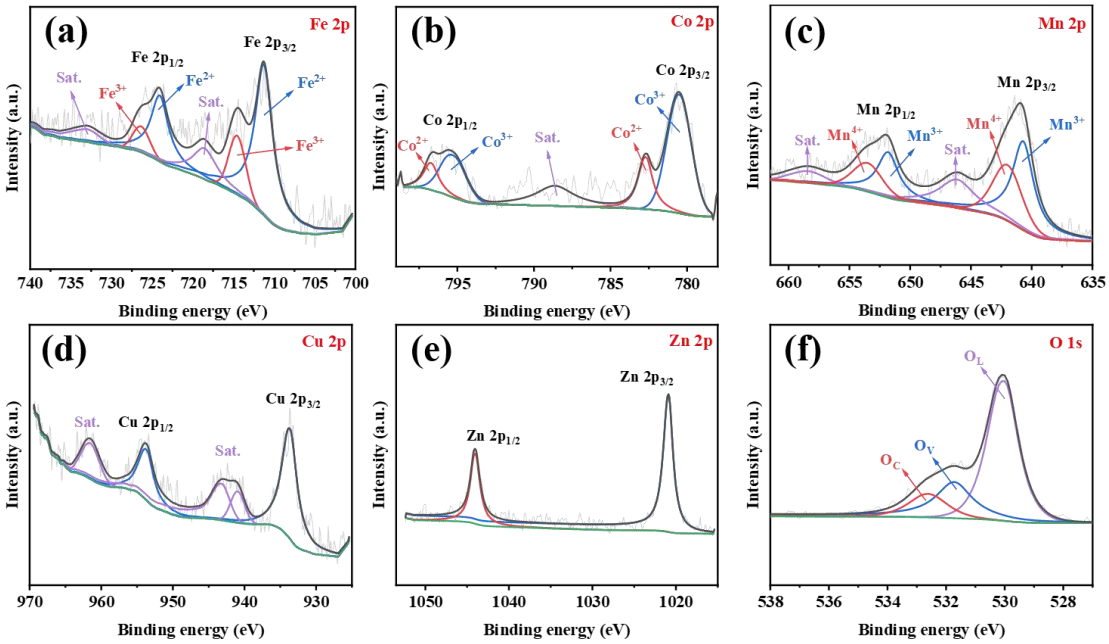


Figure 5. High-resolution XPS spectra of the 10 mmol sample: (a) Fe 2p, (b) Co 2p, (c) Mn 2p, (d) Cu 2p, (e) Zn 2p, and (f) O 1s.

The influence of precipitant type on the electrochemical performance of $(FeCoMnCuZn)_3O_4$ was evaluated in a three-electrode system. As shown in Fig. 6(a), the Na_2CO_3-derived sample exhibits the largest integrated CV area and the highest peak current density among the samples, indicating superior charge-storage capability. GCD curves collected at 1 A g^{-1} (Fig. 6(b)) further confirm this trend. The specific capacitances of the samples prepared with Na_2CO_3, $NaHCO_3$, and NaOH are calculated to be 416.4, 234.8, and 233.0 F g^{-1}, respectively. The Na_2CO_3-derived sample shows the longest discharge time and the highest specific capacitance. EIS analysis (Fig. 6(c)) shows that the Na_2CO_3-erived sample has the lowest solution resistance and a smaller charge-transfer resistance, indicating improved electron transport and interfacial charge-transfer kinetics.The effect of Na_2CO_3 dosage was further examined. As shown in Fig. 6(d), the 10 mmol

sample exhibits a significantly larger CV area than the 9 and 11 mmol samples at 100 mV s^{-1}, demonstrating the highest charge-storage capacity [35]. The GCD results (Fig. 6(e)) show that the specific capacitances of the 9, 10, and 11 mmol samples at 1 A g^{-1} are 316.4, 416.4, and 119.6 F g^{-1}, respectively. The 10 mmol sample therefore exhibits the best electrochemical performance. The Nyquist plots (Fig. 6(f)) reveal Rs values of 0.56, 0.49, and 0.64 Ω for the 9, 10, and 11 mmol samples, respectively. The lowest R_s value of the 10 mmol sample indicates favorable electrode/electrolyte interfacial contact and faster charge transport [39].

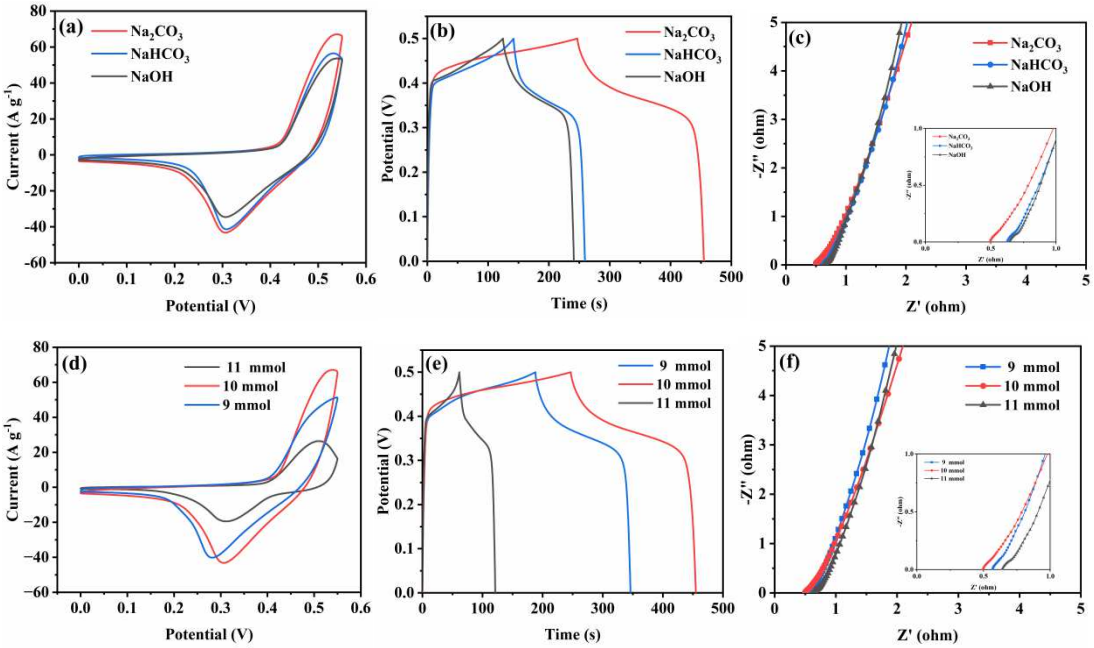


Figure 6. Electrochemical comparison of samples prepared with different precipitants and Na_2CO_3 dosages: (a) CV curves of samples prepared with different precipitants at 100 mV s^{-1}, (b) GCD curves at 1 A g^{-1}, (c) Nyquist plots, (d) CV curves of samples prepared with different Na_2CO_3 dosages at 100 mV s^{-1}, (e) GCD curves at 1 A g^{-1}, and (f) Nyquist plots.

The electrochemical behavior of the 10 mmol sample was further investigated at different scan rates and current densities. The CV curves recorded from 5 to 100 mV s^{-1} (Fig. 7(a)) show distinct redox peaks, indicating Faradaic pseudocapacitive behavior. With increasing scan rate, the

redox peaks are retained with only slight shifts, suggesting good rate response with moderate polarization at high scan rates [38]. The GCD curves (Fig. 7(b)) show clear voltage plateaus and reasonable symmetry at different current densities, further confirming the pseudocapacitive charge-storage mechanism. The discharge time decreases with increasing current density because ion diffusion and redox reactions become kinetically limited at high rates. [40] The Nyquist plot of the 10 mmol sample (Fig. 7(c)) shows an R_s value of 0.49 Ω, a small semicircle in the high-to-medium frequency region, and a steep line in the low-frequency region, indicating low internal resistance, fast charge transfer, and favorable ion diffusion kinetics.

Rate performance analysis (Fig. 7(d)) shows that the electrode delivers 416.4 F g^{-1} at 1 A g^{-1} and retains 207.4 F g^{-1} at 20 A g^{-1}, corresponding to 49.8% capacitance retention. The charge-storage kinetics were analyzed using the relationship between peak current and scan rate. The b-values of the anodic and cathodic peaks are 0.6714 and 0.6789, respectively, indicating that the charge-storage process involves both diffusion-controlled and capacitive contributions. Quantitative separation (Fig. 7(f)) shows that the diffusion-controlled contribution ratios at scan rates of 100, 80, 50, 20, 10, and 5 mV s^{-1} are 43.8%, 51.1%, 61.4%, 71.6%, 75.1%, and 76.6%, respectively. Thus, diffusion-controlled processes become more pronounced at lower scan rates, whereas capacitive behavior contributes more strongly at higher scan rates. This mixed storage mechanism is associated with the crystallinity and compact structure of the 10 mmol sample, which support bulk redox reactions while maintaining surface-accessible capacitive sites.

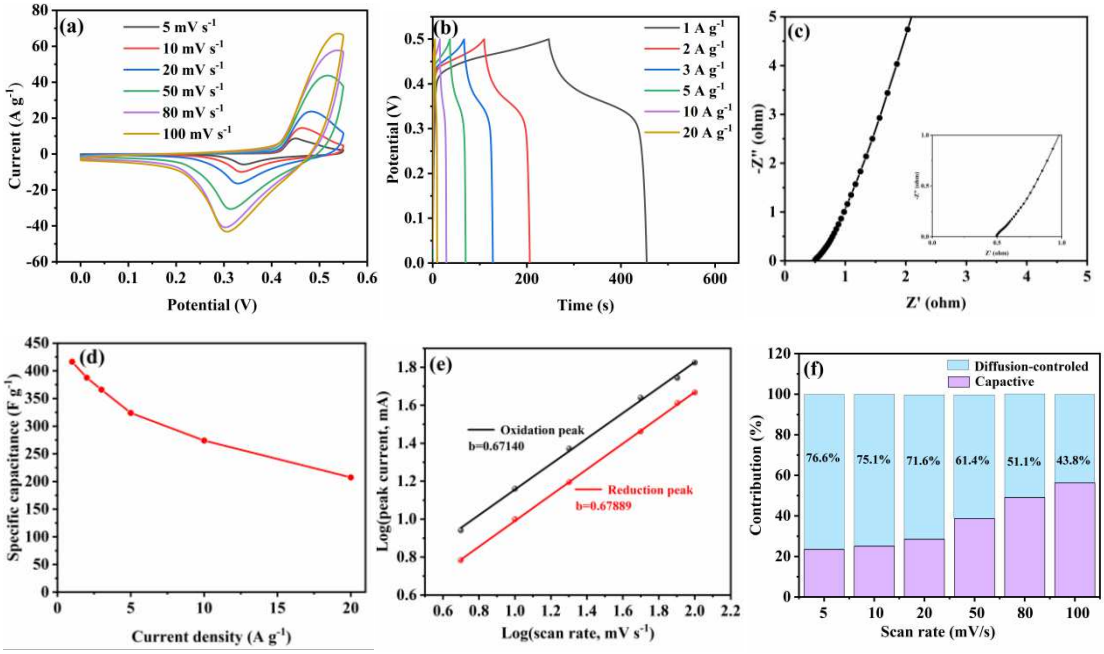


Figure 7. Electrochemical performance and kinetic analysis of the 10 mmol sample: (a) CV curves at different scan rates, (b) GCD curves at different current densities, (c) Nyquist plot, (d) rate performance, (e) relationship between peak current and scan rate, and (f) capacitive/diffusion-controlled contribution at different scan rates.

To evaluate its practical application potential, the 10 mmol $(FeCoMnCuZn)_3O_4$ sample was used as the positive electrode and activated carbon was used as the negative electrode to assemble an ASC. As shown in Fig. 8(a), the CV curves of the positive and negative electrodes show complementary potential windows, enabling the construction of a device with an extended operating voltage. CV curves measured at different voltage windows (Fig. 8(b)) show that the enclosed area increases as the voltage window expands. However, when the voltage window exceeds 1.4 V, obvious polarization is observed, suggesting possible side reactions such as electrolyte decomposition. Therefore, 1.4 V was selected as the stable working voltage window.

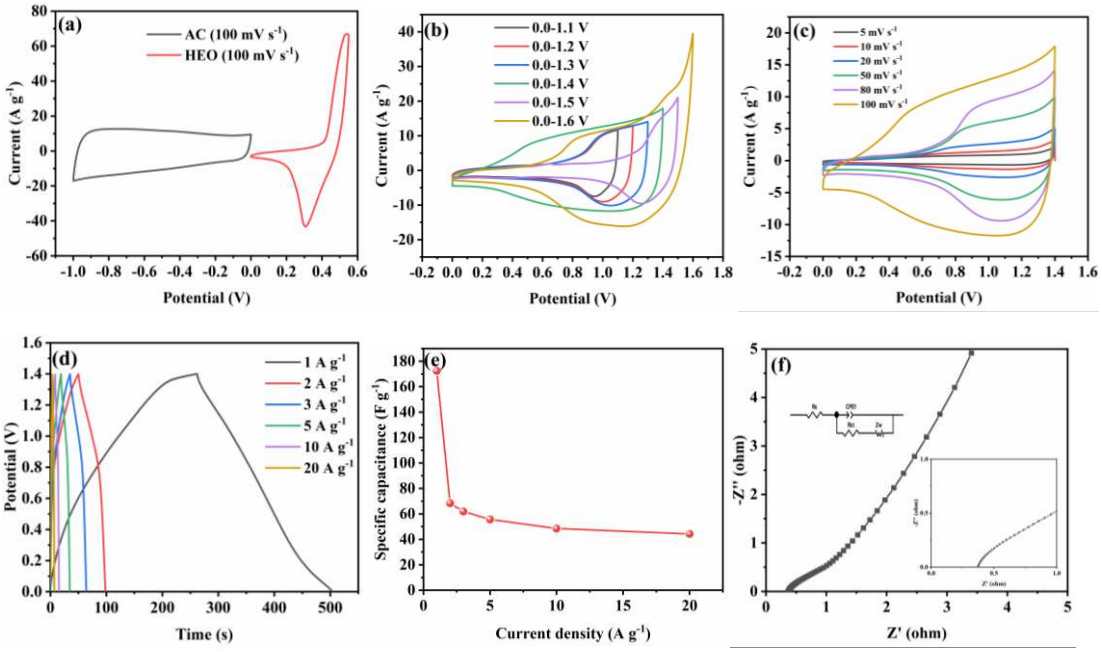
The CV curves of the ASC at scan rates of 5-100 mV s^{-1} (Fig. 8(c)) retain similar shapes with increasing scan rate, indicating good electrochemical reversibility and rate response. The remaining redox features suggest that the charge-storage behavior arises from the combined

contribution of pseudocapacitance from the HEO positive electrode and electric double-layer capacitance from the AC negative electrode [37]. The GCD curves collected from 1 to 20 A g^{-1} (Fig. 8(d)) show good symmetry and nonlinear profiles, further confirming the coexistence of Faradaic redox reactions and double-layer charge accumulation. The ASC delivers a device capacitance of 172.4 F g^{-1} at 1 A g^{-1} and retains 44.3 F g^{-1} at 20 A g^{-1} (Fig. 8(e)). EIS analysis (Fig. 8(f)) gives Rs and Rct values of 0.38 and 0.23 Ω, respectively, indicating fast charge-transfer kinetics and low ion-transport resistance.

The Ragone plot (Fig. 8(g)) shows that the ASC delivers energy densities of 46.94, 18.83, 16.86, 15.17, 13.22, and 12.06 Wh kg^{-1} at power densities of 750, 1500, 2250, 3750, 7500, and 15000 W kg^{-1}, respectively. These values compare favorably with several reported high-entropy and related transition-metal oxide devices, including (FeCoCrMnNi)C//(FeCoCrMnNi)C (3.8 Wh kg^{-1} at 1466.7 W kg^{-1}) [41], $NiCoFe_2O_4$//AC (6.4 Wh kg^{-1} at 1904.7 W kg^{-1}) [42], HEO/f-CSAC//HEO/f-CSAC (3.55 Wh kg^{-1} at 862.5 W kg^{-1}) [43], $(MnFeCoNiZn)_3O_4$//AC (7.9 Wh kg^{-1} at 750 W kg^{-1}) [44], $Co_3V_2O_8$//AC (6.19 Wh kg^{-1} at 320 W kg^{-1}) [45], $Ni_{0.8}Cu_{0.2}O$//AC (16.45 Wh kg^{-1} at 759.51 W kg^{-1})[46], and $La_{0.4}Sr_{0.6}MnO_3$//AC (16.0 Wh kg^{-1} at 929 W kg^{-1}) [34]. Cycling tests (Fig. 8(h)) show that the device retains 87.23% of its initial capacitance after 5000 cycles at 5 A g^{-1}, indicating good cycling stability and structural durability under the present testing conditions [36].

Spinel-type $(FeCoMnCuZn)_3O_4$ HEO was successfully synthesized through a coprecipitation method followed by air calcination. The effects of precipitant type and Na_2CO_3 dosage on the structure and electrochemical performance were systematically investigated. XRD results confirmed that single-phase spinel structures were obtained using different precipitants, among

which Na_2CO_3 was more favorable for improving crystallinity. Na_2CO_3-dosage optimization showed that the 10 mmol sample possessed relatively high crystallinity, uniform nanoparticle morphology, and homogeneous multimetal elemental distribution. Insufficient precipitant led to incomplete precipitation, whereas excessive precipitant promoted rapid precipitation and particle coarsening. XPS analysis revealed multivalent Fe, Co, Mn, and Cu species together with oxygen-vacancy-related defects, which contributed to enhanced pseudocapacitive reactivity and charge-transfer capability. The optimized electrode delivered 416.4 F g^{-1} at 1 A g^{-1} and retained 207.4 F g^{-1} at 20 A g^{-1}. The assembled $(FeCoMnCuZn)_3O_4$//AC ASC achieved an energy density of 46.94 Wh kg^{-1} at 750 W kg^{-1} within a 1.4 V voltage window and retained 87.23% capacitance after 5000 cycles at 5 A g^{-1}. These results demonstrate that carbonate-precipitation regulation is a feasible and low-cost strategy for tailoring high-entropy spinel oxide electrodes for supercapacitor applications.



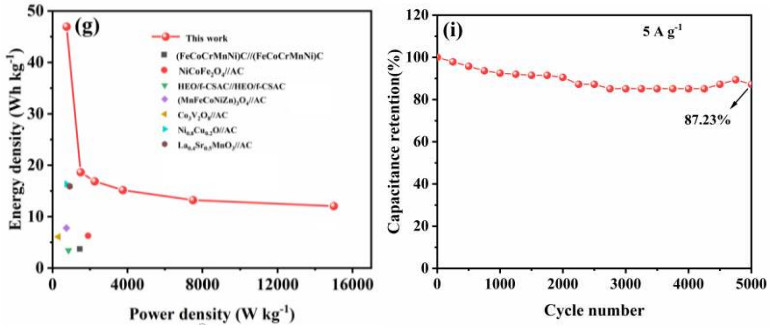


Figure 8. Electrochemical performance of the $(FeCoMnCuZn)_3O_4$//AC asymmetric supercapacitor: (a) CV curves of the positive and negative electrodes at 100 mV s^{-1}, (b) CV curves under different voltage windows, (c) CV curves at different scan rates, (d) GCD curves at different current densities, (e) rate performance, (f) Nyquist plot, (g) Ragone plot, and (h) cycling performance over 5000 cycles at 5 A g^{-1}.

Author Contributions

Tian Zijing: Writing - Review & Editing, Writing - Original Draft, Visualization, Data Curation. Zeng Fan'en: Formal Analysis & Methodology. Yuhan Liang: Project Administration, Data Management. Zilong Zhou: Investigation; Xu Bing: Writing - Review & Editing, Funding Acquisition. All authors participated in the review of the manuscript.

Declaration of Interest Statement

The authors declare that they have no known competing financial interests or personal relationships that could have appeared to influence the work reported in this paper.

Funds Provided

The authors declare that no funding, grants, or other support were received during the preparation of this manuscript.

Reference

[1] Dissanayake, K.; Kularatna-Abeywardana, D. A Review of Supercapacitors: Materials, Technology, Challenges, and Renewable Energy Applications. Journal of Energy Storage

2024, 96, 112563. https://doi.org/10.1016/j.est.2024.112563.

[2] Pathak, M.; Bhatt, D.; Bhatt, R. C.; Bohra, B. S.; Tatrari, G.; Rana, S.; Arya, M. C.; Sahoo, N. G. High Energy Density Supercapacitors: An Overview of Efficient Electrode Materials, Electrolytes, Design, and Fabrication. The Chemical Record 2023, 24 (1). https://doi.org/10.1002/tcr.202300236.

[3] Lakshmi, K. C. S.; Vedhanarayanan, B. High-Performance Supercapacitors: A Comprehensive Review on Paradigm Shift of Conventional Energy Storage Devices. Batteries 2023, 9 (4), 202. https://doi.org/10.3390/batteries9040202.

[4] Asghar, A.; Khan, K.; Hakami, O.; Alamier, W. M.; Ali, S. K.; Zelai, T.; Rashid, M. S.; Tareen, A. K.; Al-Harthi, E. A. Recent Progress in Metal Oxide-Based Electrode Materials for Safe and Sustainable Variants of Supercapacitors. Frontiers in Chemistry 2024, 12. https://doi.org/10.3389/fchem.2024.1402563.

[5] Liang, R.; Du, Y.; Xiao, P.; Cheng, J.; Yuan, S.; Chen, Y.; Yuan, J.; Chen, J. Transition Metal Oxide Electrode Materials for Supercapacitors: A Review of Recent Developments. Nanomaterials 2021, 11 (5), 1248. https://doi.org/10.3390/nano11051248.

[6] Cui, M.; Meng, X. Overview of Transition Metal-Based Composite Materials for Supercapacitor Electrodes. Nanoscale Advances 2020, 2 (12), 5516–5528. https://doi.org/10.1039/D0NA00573H.

[7] Ren, P.; Yang, G.; Jin, Y.; Peng, C.; Lei, X.; Yin, F.; Zhao, Z.; Wang, Y.; Guo, Z.; Chen, Z. High Entropy Materials as Electrode Materials for Supercapacitors: A Review. Journal of Alloys and Compounds 2025, 1024, 180153. https://doi.org/10.1016/j.jallcom.2025.180153.

[8] Sen, S.; Palabathuni, M.; Ryan, K. M.; Singh, S. High Entropy Oxides: Mapping the

Landscape from Fundamentals to Future Vistas. ACS Energy Letters 2024, 9 (8), 3694-3718. https://doi.org/10.1021/acsenergylett.4c01129.

[9] Vinnik, D. A.; Trofimov, E. A.; Zhivulin, V. E.; Zaitseva, O. V.; Zherebtsov, D. A.; Starikov, A. Y.; Sherstyuk, D. P.; Gudkova, S. A.; Taskaev, S. V. The New Extremely Substituted High Entropy (Ba,Sr,Ca,La)Fe_{6-X}(Al,Ti,Cr,Ga,In,Cu,W)xO_{19} Microcrystals with Magnetoplumbite Structure. Ceramics International 2020, 46 (7), 9656-9660. https://doi.org/10.1016/j.ceramint.2019.12.232.

[10] Nagar, S.; Sreenivasa, S. Polymer-based Supporting Materials and Polymer-encapsulated Phase Change Materials for Thermal Energy Storage: A Review on the Recent Advances of Materials, Synthesis, and Characterization Techniques. Polymer Engineering & Science 2024, 64 (9), 4341-4370. https://doi.org/10.1002/pen.26852.

[11] Khatun, M. H.; Amin, R.; Sarker, M. S. I.; Shikder, M. R.; Islam, S.; Shahjahan, M. Structural and Magnetic Properties of Fe and Ni Co-Doped SnO_2 Nanoparticles Prepared by Co-Precipitation Method. Materials Research Express 2024, 11 (1), 016102. https://doi.org/10.1088/2053-1591/ad1d87.

[12] Iriani, Y.; Suherman, B.; Sandi, D. K.; Nurosyid, F.; Khairuddin; Handoko, E.; Faquelle, D. Structural Modification and Dielectric Property of Bi-Doped $BaTiO_3$($Ba_{1-X}BiXTiO_3$) Ceramics with Co-Precipitation Technique. Integrated Ferroelectrics 2024, 240 (1), 140-148. https://doi.org/10.1080/10584587.2023.2296318.

[13] Chen, Y.-W.; Ruan, J.-J.; Ting, J.-M.; Su, Y.-H.; Chang, K.-S. Solution-Based Fabrication of High-Entropy Ba(Ti,Hf,Zr,Fe,Sn)O_3 Films on Fluorine-Doped Tin Oxide Substrates and Their Piezoelectric Responses. Ceramics International 2021, 47 (8), 11451-11458.

https://doi.org/10.1016/j.ceramint.2020.12.272.

[14] Jiang, Q.; Lu, R.; Gu, J.; Zhang, L.; Liu, K.; Huang, M.; Liu, P.; Zuo, S.; Wang, Y.; Zhao, Y. A Highly Efficient High-Entropy Metal Hydroxymethylate Electrocatalyst for Oxygen Evolution Reaction. Chemical Engineering Journal 2023, 453, 139510. https://doi.org/10.1016/j.cej.2022.139510.

[15] Nguyen, T. X.; Patra, J.; Tsai, C.; Xuan, W.; Chen, H. T.; Dyer, M. S.; Clemens, O.; Li, J.; Majumder, S. B.; Chang, J. Secondary-Phase-Induced Charge–Discharge Performance Enhancement of Co-Free High Entropy Spinel Oxide Electrodes for Li-Ion Batteries. Advanced Functional Materials 2023, 33 (30). https://doi.org/10.1002/adfm.202300509.

[16] Sushil, J.; Kumar, A.; Gautam, A.; Ahmad, M. I. High Entropy Phase Evolution and Fine Structure of Five Component Oxide (Mg, Co, Ni, Cu, Zn)O by Citrate Gel Method. Materials Chemistry And Physics 2021, 259, 124014. https://doi.org/10.1016/j.matchemphys.2020.124014.

[17] Lal, M. S.; Sundara, R. High Entropy Oxides-A Cost-Effective Catalyst for the Growth of High Yield Carbon Nanotubes and Their Energy Applications. ACS Applied Materials; Interfaces 2019, 11 (34), 30846-30857. https://doi.org/10.1021/acsami.9b08794.

[18] Shen, L.; Du, Z.; Zhang, Y.; Dong, X.; Zhao, H. Medium-Entropy Perovskites Sr(FeαTiβCoγMnζ)O_3- as Promising Cathodes for Intermediate Temperature Solid Oxide Fuel Cell. Applied Catalysis B: Environmental 2021, 295, 120264. https://doi.org/10.1016/j.apcatb.2021.120264.

[19] Stygar, M.; Dąbrowa, J.; Moździerz, M.; Zajusz, M.; Skubida, W.; Mroczka, K.; Berent, K.; Świerczek, K.; Danielewski, M. Formation and Properties of High Entropy Oxides in

Co-Cr-Fe-Mg-Mn-Ni-O System: Novel $(Cr,Fe,Mg,Mn,Ni)_3O_4$ and $(Co,Cr,Fe,Mg,Mn)_3O_4$ High Entropy Spinels. Journal of the European Ceramic Society 2020, 40 (4), 1644-1650. https://doi.org/10.1016/j.jeurceramsoc.2019.11.030.

[20] Li, D.; Liu, C.; Tao, S.; Cai, J.; Zhong, B.; Li, J.; Deng, W.; Hou, H.; Zou, G.; Ji, X. High-Entropy Electrode Materials: Synthesis, Properties and Outlook. Nano-Micro Letters 2024, 17 (1). https://doi.org/10.1007/s40820-024-01504-3.

[21] R, A. S.; Jacob, G. Exploring the Charge Storage Ability of the Spinel-Type High Entropy Oxide $(MnFeCoNiZn)_3O_4$ Nanoparticles for Supercapacitor Applications. Chemical Engineering Journal Advances 2025, 21, 100708. https://doi.org/10.1016/j.ceja.2025.100708.

[22] Kadam, R. A.; Yewale, M. A.; Teli, A. M.; Annu; Nakate, U. T.; Kumar, V.; Kadam, S. L.; Shin, D. K. Bimetallic $Co_3V_2O_8$ Microstructure: A Versatile Bifunctional Electrode for Supercapacitor and Electrocatalysis Applications. Surfaces and Interfaces 2023, 41, 103267. https://doi.org/10.1016/j.surfin.2023.103267.

[23] Chen, Y.; Mu, W.; Meng, J.; Huang, Y.; Bi, X.; Yang, R.; Lei, X.; Luo, S. Nickel-Copper Bimetallic Oxide Nanoparticles Prepared by Simple Coprecipitation Method as High Performance Electrode Materials for Asymmetric Supercapacitors. Langmuir 2024, 40 (36), 19239-19250. https://doi.org/10.1021/acs.langmuir.4c02454.

[24] Talluri, B.; Aparna, M. L.; Sreenivasulu, N.; Bhattacharya, S. S.; Thomas, T. High Entropy Spinel Metal Oxide $(CoCrFeMnNi)_3O_4$ Nanoparticles as a High-Performance Supercapacitor Electrode Material. Journal of Energy Storage 2021, 42, 103004. https://doi.org/10.1016/j.est.2021.103004.

[25] Zhang, D.; Xu, S.; Li, T.; Zhang, M.; Qi, J.; Wei, F.; Meng, Q.; Ren, Y.; Cao, P.; Sui, Y.

High-Entropy Oxides Prepared by Dealloying Method for Supercapacitors. 2023, 1 (2), 780-789. https://doi.org/10.1021/acsaenm.2c00198.

[26] Yin, Y.; Zhang, W.-B.; Chen, B.; Feng, J.; Yang, J.-L.; Yang, Z.-Q.; Li, J.-J.; Ma, X.-J. Porous Powder Synthesis of $(FeCoCrMnNi)_3O_4$ High Entropy Ceramic and Its Supercapacitor Applications. Ceramics International 2024, 50 (7), 10292–10304. https://doi.org/10.1016/j.ceramint.2023.12.341.

[27] Wang, Y.; Liu, J.; Cao, H.; Ding, J.; Wang, N.; He, C.; Zhang, Y. Facile Synthesis of Porous High-Entropy Perovskite Nanoparticles through MOF Gel Method for Solid-State Supercapacitor Application. Chemical Engineering Journal 2025, 509, 161246. https://doi.org/10.1016/j.cej.2025.161246.

[28] Chandra Mohanty, G.; Das, S.; Verma, A. Synthesis of $(FeCoNiCuMn)_3O_4$ Spinel-High Entropy Oxide and Green Carbon from Agricultural Waste for Supercapacitor Application. RSC Advances 2024, 14 (46), 33830-33842. https://doi.org/10.1039/D4RA05204H.

[29] Xu, B.; Yang, Q.; Zeng, F.; Zhu, S.; Sun, Y.; Zhang, Z.; Tian, Z.; Shen, Y. Effect of Precipitant Selection on High Entropy $(CrMnFeCoNi)_3O_4$ Nanoparticles for Superior-Performance Supercapacitors. Ionics 2026. https://doi.org/10.1007/s11581-026-07071-4.

[30] Patel, A.; Patel, S. K.; Singh, R. S.; Patel, R. P. Review on Recent Advancements in the Role of Electrolytes and Electrode Materials on Supercapacitor Performances. 2024, 19 (1). https://doi.org/10.1186/s11671-024-04053-1.

[31] Xu, J.; Sun, Y.; Lu, M.; Wang, L.; Zhang, J.; Tao, E.; Qian, J.; Liu, X. Fabrication of the Porous $MnCo_2O_4$ Nanorod Arrays on Ni Foam as an Advanced Electrode for Asymmetric

Supercapacitors. Acta Materialia 2018, 152, 162–174. https://doi.org/10.1016/j.actamat.2018.04.025.

[32] Chen, M.; Chen, D.; Liao, Y.; Zhong, X.; Li, W.; Zhang, Y. Layered Lithium-Rich Oxide Nanoparticles Doped with Spinel Phase: Acidic Sucrose-Assistant Synthesis and Excellent Performance as Cathode of Lithium Ion Battery. ACS Applied Materials & Interfaces 2016, 8 (7), 4575-4584. https://doi.org/10.1021/acsami.5b10219.

[33] Zeng, F.; Xu, B.; Zhang, Z.; Yang, Q.; Sun, Y.; Li, C.; Li, G. Synthesis of Porous High-Entropy Spinel Oxide $(CrMnFeCoNi)_3O_4$ for High–Performance Supercapacitors. Journal of Energy Storage 2026, 150, 120056. https://doi.org/10.1016/j.est.2025.120056.

[34] Madhale, K. V.; Faras, M. M.; Mohite, A. A.; Shembade, U. V.; Gurav, S. R.; Torane, A. P.; Kulkarni, S. B. Facile Combustion Synthesis of Granular-like La1-xSrxMnO_3 Perovskites as Electrode Material for Supercapacitor Application. Journal of Energy Storage 2024, 101, 113841. https://doi.org/10.1016/j.est.2024.113841.

[35] Shahid, A.; Kayani, Z. N.; Nazli, H.; Riaz, S.; Naseem, S. Controllable Synthesis of Composite Electrode Material to Enhance the Electrochemical Performance of Supercapacitors. Optical Materials 2023, 143, 114264. https://doi.org/10.1016/j.optmat.2023.114264.

[36] Tamboli, M. S.; Zuhaib, H.; Truong, N. T. N.; Tamboli, A. M.; Park, H.; Alshehri, S.; Shinde, S. K.; Park, C. Boosting Supercapacitive Performance of CuxZn1-xO Electrodes with Enhanced Specific Capacitance and Long-Term Stability. Inorganic Chemistry Communications 2025, 177, 114392. https://doi.org/10.1016/j.inoche.2025.114392.

[37] Shakoor, M.; Ali, G.; Kubra, K. T.; Butt, A.; Iqbal, F.; Zehra, S.; Nadeem, M.

Electrochemical Investigations of Fe_3O_4/ZnO/Carbon Ternary Composite Derived from Bimetallic Metal-Organic Framework for Supercapacitor Applications. Inorganic Chemistry Communications 2025, 182, 115586. https://doi.org/10.1016/j.inoche.2025.115586.

[38] Pedro Aguiar dos Santos, J.; Cesar Rufino, F.; Yutaka Ota, J. I.; Fernandes, R. C.; Vicentini, R.; Pagan, C. J. B.; Morais Da Silva, L.; Zanin, H. Best Practices for Electrochemical Characterization of Supercapacitors. Journal of Energy Chemistry 2023, 80, 265-283. https://doi.org/10.1016/j.jechem.2022.12.034.

[39] Kshetri, T.; Singh, T. I.; Lee, Y. S.; Khumujam, D. D.; Kim, N. H.; Lee, J. H. Metal Organic Framework-Derived Cobalt Telluride-Carbon Porous Structured Composites for High-Performance Supercapacitor. Composites Part B: Engineering 2021, 211, 108624. https://doi.org/10.1016/j.compositesb.2021.108624.

[40] Ze, H.; Fan, X.-T.; Yang, Z.-L.; Ding, X.; A, Y.-L.; Wen, X.; Zhang, Y.; Oropeza, F. E.; Zhang, K. H. L.; Gu, Y. Deciphering the Competitive Charge Storage Chemistry of Metal Cations and Protons in Aqueous MnO_2-Based Supercapacitors. Journal of the American Chemical Society 2025, 147 (11), 9620-9628. https://doi.org/10.1021/jacs.4c17458.

[41] Zhang, X.-L.; Zhang, W.-B.; Yin, Y.; Theint, M. M.; Guo, S.-B.; Chai, S.-S.; Zhou, X.; Ma, X.-J. Sol-Gel Method Preparation and High-Rate Energy Storage of High-Entropy Ceramic (FeCoCrMnNi)C Porous Powder. Ceramics International 2023, 49 (17), 29327–29338. https://doi.org/10.1016/j.ceramint.2023.06.228.

[42] Mayakkannan, M.; Murugan, A.; Shameem, A.; Siva, V.; Sasikumar, S.; Thangarasu, S.; Bahadur, S. A. Investigations on Ternary Transition Metal Ferrite: $NiCoFe_2O_4$ as Potential Electrode for Supercapacitor Prepared by Microwave Irradiation Method. Journal of Energy

Storage 2021, 44, 103257. https://doi.org/10.1016/j.est.2021.103257.

[43] Lal, M. S.; Sundara, R. Multifunctional High Entropy Oxides Incorporated Functionalized Biowaste Derived Activated Carbon for Electrochemical Energy Storage and Desalination. Electrochimica Acta 2022, 405, 139828. https://doi.org/10.1016/j.electacta.2021.139828.

[44] R, A. S.; Jacob, G. Exploring the Charge Storage Ability of the Spinel-Type High Entropy Oxide $(MnFeCoNiZn)_3O_4$ Nanoparticles for Supercapacitor Applications. Chemical Engineering Journal Advances 2025, 21, 100708. https://doi.org/10.1016/j.ceja.2025.100708.

[45] Chen, Y.; Mu, W.; Meng, J.; Huang, Y.; Bi, X.; Yang, R.; Lei, X.; Luo, S. Nickel–Copper Bimetallic Oxide Nanoparticles Prepared by Simple Coprecipitation Method as High Performance Electrode Materials for Asymmetric Supercapacitors. LANGMUIR 2024, 40 (36), 19239-19250. https://doi.org/10.1021/acs.langmuir.4c02454.

[46] Rahmati, B.; Hakimi, M.; Hajzadeh, I.; Sanaee, Z.; Mohseni, S. M. Urchin-like Structure and Nanowire Arrays of $NiCo_2O_4/NiCoSe_2$ as a Binder-Free Electrode Material for High-Performance Supercapacitor. Materials Science In Semiconductor Processing 2024, 171, 108002. https://doi.org/10.1016/j.mssp.2023.108002.